

New reconstruction of event-integrated spectra (spectral fluences) for major solar energetic particle events [★]

S. Koldobskiy^{1,2,3}, O. Raukunen⁴, R. Vainio⁴, G.A. Kovaltsov⁵, and I. Usoskin^{1,2}

¹ University of Oulu, Finland

² National Research Nuclear University MEPhI, Moscow, Russia

³ St. Petersburg State University, Russia

⁴ University of Turku, Finland

⁵ A.F. Ioffe Physical-Technical Institute of Russian Academy of Sciences, St.Petersburg, Russia

ABSTRACT

Aims. Fluences of solar energetic particles (SEPs) are not easy to evaluate, especially for high-energy events (i.e. ground-level enhancements, GLEs). Earlier estimates of event-integrated SEP fluences for GLEs were based on partly outdated assumptions and data, and they required revisions. Here, we present the results of a full revision of the spectral fluences for most major SEP events (GLEs) for the period from 1956–2017 using updated low-energy flux estimates along with greatly revisited high-energy flux data and applying the newly invented reconstruction method including an improved neutron-monitor yield function.

Methods. Low- and high-energy parts of the SEP fluence were estimated using a revised space-borne/ionospheric data and ground-based neutron monitors, respectively. The measured data were fitted by the modified Band function spectral shape. The best-fit parameters and their uncertainties were assessed using a direct Monte Carlo method.

Results. A full reconstruction of the event-integrated spectral fluences was performed in the energy range above 30 MeV, parametrised and tabulated for easy use along with estimates of the 68% confidence intervals.

Conclusions. This forms a solid basis for more precise studies of the physics of solar eruptive events and the transport of energetic particles in the interplanetary medium, as well as the related applications.

Key words. Sun:particle emission - Sun:activity - Sun:flares - solar-terrestrial relations

1. Introduction

In addition to Galactic cosmic rays (GCR) continuously bombarding the Earth with slightly variable flux, sporadic solar eruptive events, such as flares and/or coronal mass ejections (CMEs) may cause dramatic (by many orders of magnitude) enhancements of energetic particle fluxes near Earth, which are called solar energetic particle (SEP) events (Vainio et al. 2009; Desai & Giacalone 2016; Klein & Dalla 2017). SEP events occur quite frequently during maxima and early declining phases of solar-activity cycles and very seldom during the minimum phase (e.g. Bazilevskaya et al. 2014). Sometimes, eruptive events can be sufficiently energetic to accelerate particles to relatively high energy (>400 MeV) so that they can penetrate the Earth's magnetosphere and atmosphere, inducing atmospheric nucleonic cascades, which can be measured by ground-based detectors (e.g. Shea & Smart 2012). Such events are known as ground-level enhancements (GLEs), which are consequently numbered from #1, which took place in February 1942, to the most recent #72 in September 2017. The first four GLEs were recorded by ionisation chambers (Forbush 1946) and cannot be quantitatively assessed, but those starting from GLE #5 (23-Feb-1956) were recorded by the network of ground-based neutron monitors (NMs) with a possibility of quantifying their intensities and spectral parameters (e.g. Mishev et al. 2018). All available information of NM data for GLEs #5–72 is collected in the International GLE Database¹ (IGLED, see Usoskin et al. 2020b).

Studies of SEP events are important for different reasons. On one hand, solar eruptive events are well-observed processes of energetic-particle acceleration (Vainio & Afanasiev 2018), which can be studied in detail using a multi-messenger approach, complementing particle data with observations in different wavelengths (e.g., Plainaki et al. 2014; Cliver 2016; Kocharov et al. 2017). For this purpose, the peak flux intensity and detailed temporal variability of the particle flux are important as signatures of the acceleration process in the solar corona and the interplanetary medium (e.g. Desai & Giacalone 2016; Kong et al. 2017). Accordingly, numerous studies were focused on peak fluxes of SEPs and corresponding acceleration and transport processes (e.g. Kouloumvakos et al. 2015; Kocharov et al. 2017). On the other hand, enhanced fluxes of energetic particles affect the radiation environment near the Earth (e.g. Webber et al. 2007; Mishev et al. 2015), making not only the peak fluxes but also the fluence (event-integrated flux) and its spectral shape of significant importance, especially for extreme events (e.g. Cliver et al. 2020). We emphasise that SEP fluences can not be used for the detailed study of SEP acceleration processes, because (i) the observations at 1 AU are also modified by transport, and (ii) different energies in the fluence spectrum can be dominated by different acceleration mechanisms or by the same mechanism operating under different conditions. It is evident from the proton time-intensity profiles alone that the fluence at MeV and 10-MeV energies is often dominated by acceleration at interplanetary shocks (e.g. Reames 1999). However, the question is more open at 100-MeV and GeV energies peaking much earlier, with possible contributions from flares and/or coronal shocks as the

¹ <https://gle.oulu.fi>

main candidates to account for the acceleration (see Cliver 2016 and references therein). Even if the same CME-driven shock were responsible for the acceleration of 10-MeV and 1-GeV protons, the former would typically be accelerated mainly in the solar wind and the latter in the corona, and there is no reason to suggest that the spectral form of the fluence would reveal something common about the accelerator properties.

Composing an event-integrated energy (or rigidity) spectrum (spectral fluence) of a SEP event is a difficult task. Direct measurements of the spectrum covering the high-energy (>400 MeV) range can be done with modern space-borne magnetic spectrometers PAMELA (Payload for Antimatter Matter Exploration and Light-nuclei Astrophysics – Adriani et al. 2014) operated from 2006–2016, and AMS-02 (Alpha Magnetic Spectrometer – Aguilar et al. 2018), which has been in operation since 2011. SEP events analysed using PAMELA data were presented by Bruno et al. (2018), while data from AMS-02 are not available yet (Bindi 2017). However, these instruments are located aboard low-orbiting satellites, and thus spend most of their time inside the Earth’s magnetosphere and can detect low-energy solar particles only intermittently (5–10 minutes per half-orbit), leading to essential uncertainties in both SEP peak fluxes and fluences, especially for impulsive events. Additionally, uncertainties of the SEP fluxes were large during the earlier years (e.g. Reeves et al. 1992; Tylka et al. 1997) due to the saturation of the detectors by strong particle fluxes and the possible penetration of high-energy particles into the detector through the walls of the collimator, leading to an enhanced effective acceptance.

Thus, for most of the events, one has to combine data from different instruments, including low-energy (<400 MeV) space-borne detectors located beyond the magnetosphere, and energy-integrating (above 400 MeV) ground-based NMs. The reconstruction of the spectrum is typically done by fitting a prescribed spectral shape to the data and finding the best-fit parameters of this shape along with their uncertainties. The first consistent reconstruction of combined spectral fluences for major GLE events was made by Tylka & Dietrich (2009) and updated by Raukunen et al. (2018). It was based on a combination of lower-energy data from different space-borne detectors and the high-energy tail based on ground-based NM datasets. The spectral fluence was estimated by fitting the Band-function spectral shape (double power law with an exponential junction – Band et al. 1993) to the integral rigidity spectral fluence. The space-borne data were collected from different sources, while NM data were analysed by applying the NM yield-function by Clem & Dorman (2000). Spectral fluences were presented as tabulated parameters of the Band-function approximation for each GLE event. This dataset has been extensively used in numerous studies for solar and space physics (Cliver et al. 2020; Anastasiadis et al. 2019; Herbst et al. 2019), but it has become obsolete and requires an essential revision. First, the high-energy space-borne data have been essentially revisited and corrected for known errors (Raukunen et al. 2020). Second, the data of the NM network for all GLE events have been revisited (Usoskin et al. 2020b): apparent errors were corrected, and the variable GCR background was taken into account. Furthermore, a most recent and directly verified using AMS-02 data NM yield function (Mishev et al. 2013, 2020) and a new effective-energy analysis method were developed (Koldobskiy et al. 2018, 2019). Moreover, the Band function is not an optimum parametric shape for the GLE energy (or rigidity) spectrum, which requires a roll-off at the highest energies. Here, we present a complete revision of the reconstructions of the SEP spectral fluences for major SEP events (with GLE) using most up-to-date knowledge of the SEP measure-

ments on ground and in space, new models, and a modified spectral form including a roll-off at high energies.

2. Datasets

All sources of the energy/rigidity integral fluences used in this study are described below.

2.1. Space-borne and ionospheric data

Data for the rigidities below 1 GV (energy <430 MeV) were taken from space-borne or ionospheric (in the pre-satellite era) data. For the period since 1989 (i.e. GLEs # 40–72), we used all publicly available data from the GOES (Geostationary Operational Environmental Satellite) energetic particle sensor (EPS) and high energy proton and alpha detector (HEPAD) datasets² (Onsager et al. 1996; Sellers & Hanser 1996). The fluences at the low-energy channels in this study, that is, >30 MeV, >50 MeV, >60 MeV, and >100 MeV, were calculated directly from the EPS dataset, but the higher energy HEPAD data were revised using a so-called bow-tie method (Van Allen et al. 1974). The nominal HEPAD channels are wide in energy, and they have responses that vary significantly within the channels, and in some cases even outside the nominal channel range. In the bow-tie analysis, calibrated channel responses were folded with an assumed spectral form (power-law), and by varying the spectral index within a realistic range for SEP events, optimal effective-energy and geometric-factor values were found for each channel. The method is explained in full detail in Raukunen et al. (2020). In addition, the cleaning of data spikes (single points with spuriously increased flux) and background subtraction was performed on both GOES datasets. We note that energy bounds of the HEPAD channels changed slightly after 1995 (GLE # 53) due to differences in the calibration procedures used for GOES-6 (until 1995) and GOES-8 onwards (after 1995). GLEs # 71 and 72 were measured by GOES-13, with 10–100 MeV channels represented by two detectors facing east and west, so that the fluences were taken as the average of these two measurements. Resulting omnidirectional fluences (in units of 10^5 cm^{-2}) are presented in Table 1. Data channels with rigidity above 1 GV were not used in the fitting procedure (Section 3) because of their lower reliability.

We also used the SEP spectrum measured by the PAMELA experiment³ (Bruno et al. 2018) for the GLE #71 (17-May-2012). For years before 1989, we used fluences from several sources based on different spacecraft and experiments (King 1974; Reedy 1977; Goswami et al. 1988; Feynman & Gabriel 1990; Jun et al. 2007; Webber et al. 2007). The exact sources of the low-energy data for each event are specified in the legends of the panels of the figure in Appendix A.

2.2. Ground-based data

Data for rigidity above 1 GV (energy >430 MeV) were used from a recent reconstruction of SEP fluences based on the de-trended data of the NM network from IGLED (Usoskin et al. 2020b). For some events and some NMs (mostly low-latitude ones), only an upper limit of the enhancement can be set (see vertical blue bars in Figure 1). A robust estimation of the SEP fluence using NM data requires the accurate identification of

² <https://www.ngdc.noaa.gov/stp/satellite/goes/index.html>

³ Experimental data is available at the SSDC cosmic ray database: <https://tools.ssdsc.asi.it/CosmicRays/>.

Table 1. Event-integrated omnidirectional integral fluences $F(> E)$ (in units of 10^5 cm^{-2}) obtained here for GLEs # 40–72. Columns 1–5 provide the GLE number, source of data, start date and time of the event, day of the GCR background calculation (BG; BG year is the same as for start date and is not shown), and the integration time (IT). Columns 6–13 provide the $F(> E)$ values. Energies E for different channels are given in MeV. Uncertainties include only statistical, background subtraction, and bow-tie-method errors, while systematic and instrumental errors are not considered. Errors smaller than 1% are not shown. $F(> 10)$ and $F(> 462/486)$ channels are not used in the fitting procedure.

GLE #	Source of data	Start date and time UT	BG	IT, h	$F(> E), 10^5 \text{ cm}^{-2}$							
					10	30	50	60	100	336	395	486
40	GOES-6	08:00 25/07/1989	24/07	24	91.79	68.36	53.83	43.95	19.74	1.90 ^{+0.06} _{-0.06}	0.99 ^{+0.06} _{-0.09}	0.57 ^{+0.03} _{-0.05}
41	GOES-6	00:00 16/08/1989	24/07	24	5024	1666	912.9	638.9	227.3	21.24 ^{+0.39} _{-0.37}	10.44 ^{+0.45} _{-0.84}	5.83 ^{+0.22} _{-0.44}
42	GOES-6	11:00 29/09/1989	28/09	22	10387	7159	5330	4158	1672	145.82 ^{+2.63} _{-2.49}	69.48 ^{+5.56} _{-4.11}	40.51 ^{+1.46} _{-3.00}
43	GOES-6	12:00 19/10/1989	28/09	24	6897	4104	3628	3164	1480	113.20 ^{+2.05} _{-1.94}	51.33 ^{+2.21} _{-4.11}	27.74 ^{+1.00} _{-2.06}
44	GOES-6	17:00 22/10/1989	28/09	24	16241	8199	5373	3741	1149	54.84 ^{+1.00} _{-0.94}	22.15 ^{+0.96} _{-1.78}	11.30 ^{+0.41} _{-0.84}
45	GOES-6	17:00 24/10/1989	28/09	24	7938	3675	2721	2074	839.2	101.70 ^{+1.84} _{-1.74}	53.11 ^{+2.28} _{-4.25}	31.69 ^{+1.15} _{-2.35}
46	GOES-6	06:00 15/11/1989	14/11	24	55.44	43.31	39.86	35.47	15.26	1.31 ^{+0.05} _{-0.05}	0.67 ^{+0.04} _{-0.06}	0.36 ^{+0.03} _{-0.03}
47	GOES-6	22:00 21/05/1990	05/05	24	477.7	271.0	213.5	173.8	72.84	6.31 ^{+0.13} _{-0.12}	3.00 ^{+0.14} _{-0.24}	1.68 ^{+0.07} _{-0.13}
48	GOES-6	20:00 24/05/1990	05/05	24	317.8	235.3	211.8	185.0	90.80	12.07 ^{+0.23} _{-0.22}	6.13 ^{+0.27} _{-0.26}	3.65 ^{+0.14} _{-0.27}
49	GOES-6	20:00 26/05/1990	05/05	24	182.3	144.7	131.0	114.5	55.14	6.49 ^{+0.13} _{-0.13}	3.25 ^{+0.13} _{-0.26}	1.90 ^{+0.08} _{-0.14}
50	GOES-6	04:00 28/05/1990	05/05	24	124.5	102.7	90.42	77.23	37.57	4.38 ^{+0.10} _{-0.09}	2.15 ^{+0.10} _{-0.18}	1.27 ^{+0.05} _{-0.10}
51	GOES-6	01:00 11/06/1991	31/07	11	894.3	559.2	397.3	276.7	80.81	4.09 ^{+0.09} _{-0.08}	1.79 ^{+0.08} _{-0.15}	1.04 ^{+0.04} _{-0.08}
52	GOES-6	08:00 15/06/1991	31/07	24	2883	1215	819.2	595.8	207.3	17.16 ^{+0.32} _{-0.30}	8.03 ^{+0.35} _{-0.65}	4.54 ^{+0.17} _{-0.34}
53	GOES-6	19:00 25/06/1992	24/06	24	680.7	216.9	131.4	88.45	27.69	2.31 ^{+0.07} _{-0.07}	1.08 ^{+0.06} _{-0.10}	0.63 ^{+0.04} _{-0.05}

$F(> E), 10^5 \text{ cm}^{-2}$												
					10	30	50	60	100	337	392	462
55	GOES-8	12:00 06/11/1997	01/11	24	3165	1248	652.5	496.6	226.7	15.63 ^{+0.13} _{-0.12}	8.54 ^{+0.24} _{-0.48}	5.42 ^{+0.13} _{-0.24}
56	GOES-8	13:00 02/05/1998	15/05	24	471.8	162.8	77.84	57.32	24.60	1.47 ^{+0.06} _{-0.05}	0.76 ^{+0.05} _{-0.06}	0.51 ^{+0.04} _{-0.04}
58	GOES-8	20:00 24/08/1998	16/08	18	683.3	111.6	43.01	31.25	13.18	1.20 ^{+0.05} _{-0.04}	0.72 ^{+0.04} _{-0.06}	0.42 ^{+0.03} _{-0.04}
59	GOES-8	10:00 14/07/1900	10/07	18	47291	18726	7519	4657	1561	59.94 ^{+0.38} _{-0.33}	30.26 ^{+0.82} _{-1.70}	17.65 ^{+0.40} _{-0.76}
60	GOES-8	13:00 15/04/2001	24/03	24	4510	1352	728.0	583.3	302.2	46.07 ^{+0.30} _{-0.26}	28.30 ^{+0.77} _{-1.59}	19.24 ^{+0.43} _{-0.83}
61	GOES-8	02:00 18/04/2001	24/03	24	1509	382.5	168.9	125.0	54.70	6.57 ^{+0.07} _{-0.07}	4.13 ^{+0.12} _{-0.12}	2.82 ^{+0.07} _{-0.13}
62	GOES-8	16:00 04/11/2001	03/11	24	23264	6919	2366	1307	339.9	9.47 ^{+0.09} _{-0.08}	4.20 ^{+0.12} _{-0.24}	2.28 ^{+0.06} _{-0.11}
63	GOES-8	04:00 26/12/2001	25/12	24	3129	790.6	326.4	218.1	77.38	3.25 ^{+0.05} _{-0.05}	1.65 ^{+0.06} _{-0.10}	0.99 ^{+0.04} _{-0.05}
64	GOES-8	01:00 24/08/2002	10/08	24	2273	430.8	178.2	126.5	50.59	3.46 ^{+0.05} _{-0.05}	1.81 ^{+0.06} _{-0.11}	1.17 ^{+0.04} _{-0.06}
65	GOES-10	11:00 28/10/2003	21/10	19	55516	19857	7083	3932	979.1	20.12 ^{+0.15} _{-0.13}	10.02 ^{+0.28} _{-0.56}	5.88 ^{+0.14} _{-0.26}
66	GOES-10	20:00 29/10/2003	21/10	14	8614	2847	1265	889.9	342.0	15.76 ^{+0.12} _{-0.11}	8.18 ^{+0.23} _{-0.46}	4.83 ^{+0.12} _{-0.21}
67	GOES-10	17:00 02/11/2003	21/10	24	5729	1367	461.0	280.4	91.91	5.13 ^{+0.06} _{-0.06}	2.73 ^{+0.09} _{-0.16}	1.63 ^{+0.05} _{-0.08}
69	GOES-11	06:00 20/01/2005	12/01	24	6977	3572	2116	1656	785.4	106.83 ^{+0.67} _{-0.56}	63.81 ^{+1.73} _{-3.58}	39.16 ^{+0.87} _{-1.69}
70	GOES-11	02:00 13/12/2006	04/12	24	3550	1553	796.3	569.7	227.1	15.22 ^{+0.12} _{-0.11}	9.04 ^{+0.23} _{-0.51}	5.64 ^{+0.14} _{-0.25}
71	GOES-13	01:00 16/05/2012	15/05	24	685.2	243.7	123.8	92.11	39.26	2.32 ^{+0.05} _{-0.05}	1.80 ^{+0.07} _{-0.11}	1.22 ^{+0.03} _{-0.07}
72	GOES-13	16:00 10/09/2017	02/09	24	9315	3383	1509	1048	395.0	11.45 ^{+0.10} _{-0.09}	7.50 ^{+0.22} _{-0.43}	4.37 ^{+0.11} _{-0.20}

the GLE signal itself. Since GLEs # 6, 7, 9, 14, 15, 17, 34, 54, 57, and 68 were weak and lacking sufficiently clear signals, we did not analyse these events. Originally, the SEP event integration period was deduced from high-energy NM de-trended data (Usoskin et al. 2020b) and was applied to the low-energy data where we had this opportunity (i.e. starting from GLE #40). For earlier GLEs, we used all available data, which sometimes have bigger integration periods. It was taken into account as an additional uncertainty in Step 2 below.

3. Fitting procedure

For each event, the integral fluence points in both high-energy (Section 2.2) and low-energy (Section 2.1) ranges were fitted with a prescribed spectral shape, as described below. Here, we used a modified Band function (MBF), which includes an exponential roll-off term, similar to the Ellison-Ramaty spectral shape

(Ellison & Ramaty 1985):

$$F(R) = J_1 \left(\frac{R}{1\text{GV}} \right)^{-\gamma_1} \exp\left(-\frac{R}{R_1}\right) \text{ if } R < R_b, \quad (1)$$

$$F(R) = J_2 \left(\frac{R}{1\text{GV}} \right)^{-\gamma_2} \exp\left(-\frac{R}{R_2}\right) \text{ if } R \geq R_b, \quad (2)$$

where $F(R) \equiv f(> R)$ is the omnidirectional fluence (in units of cm^{-2}) of particles with a rigidity greater than R , R is expressed in gigavolts, parameters $\gamma_1, \gamma_2, R_1, R_2$, and J_2 are defined by fitting, and other parameters can be calculated as

$$R_b = \gamma_0 \cdot R_0 \quad (3)$$

$$J_1 = J_2 \cdot R_b^{-\gamma_0} \cdot \exp(\gamma_0)$$

$$\gamma_0 = \gamma_2 - \gamma_1$$

$$R_0 = R_1 \cdot R_2 / (R_2 - R_1).$$

This function is constructed in such a way that it and its first derivative are continuous, providing a smooth junction between the two parts. We used a fitting method based on a three-step Monte Carlo procedure further developed after Usoskin et al. (2020b), as illustrated in Figure 1. The method includes L Monte Carlo iterations.

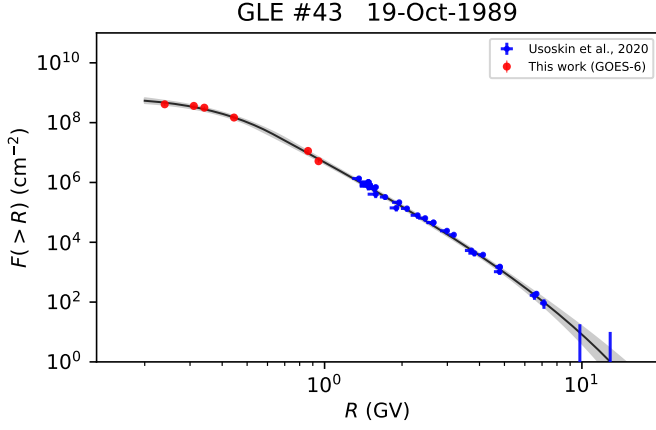


Fig. 1. Example of the fitting of the modified Band function (Equations 1–2) to the data points (Section 3) for GLE #43, 19-Oct-1989. Blue crosses and vertical lines denote the high-energy NM data with uncertainties, and the upper limits, respectively, (Usoskin et al. 2020b), while red circles correspond to low-energy data from GOES-6 (see Table 1). The grey line with shading depicts the best-fit MBF, along with its 68% confidence interval.

Step 1: Fitting the high-energy (NM) part

First, we fitted the high-energy part of the spectral shape (Equation 2) using the data from the NM network (blue crosses in Figure 1) for each event with M spectral points with uncertainties, and m points, corresponding to the upper limits of the fluence (vertical blue lines in the figure). The uncertainties are both statistical (count-rate statistic) and systematic, related to the ‘effective-rigidity’ (or bow-tie) method ones. For the l -th iteration, we simulated a set of randomised ‘exact’ fluence $F^*(R^*)$ values, applying the same procedure as in Usoskin et al. (2020b), so that for each point k ($1..M$) the value of R_k^* was randomly and uniformly taken inside R_k error bars; the value of $F_k^*(> R)$ was computed using Equation (4) from Usoskin et al. (2020b), where the scaling factor K_k was randomly taken inside the error bars using the uniform distribution, and the GLE integral intensity X_k (in units of %·hr above the GCR background over the entire duration of the event, see Asvestari et al. (2017)) was randomly taken inside the error bars, defined as $\sigma_{X_k} = \max[1; 0.1 \cdot X_k]$ %·hr using the normal distribution. In order to avoid a bias towards more numerous polar NMs during the fitting procedure, we considered only one randomly selected point (NM) in each rigidity bin of 0.4 GV widths. For several weak events (# 18, 35, 53, 58, 63, 64), the bin width was reduced to 0.1 GV to keep the number of fitted points reasonable. We checked that reducing the bin size does not lead to any significant bias in the results. Then, this set of points $F^*(R^*)$ was fitted by the spectral shape (Equation 2) applying a non-linear least-squares method (scipy.optimize.curve_fit function in Python), and the best-fit parameters J_2 , γ_2 and R_2 were found based on the minimisation of the logarithmic residual D :

$$D \equiv \min \left[\sum (\log(F_{\text{fit}}(R^*)) - \log(F^*(R^*)))^2 \right], \quad (4)$$

where F_{fit} is the value computed using the fit-function (Equation 2) for the rigidity R^* . We additionally checked that the obtained best-fit parameters are physically reasonable, that is, the obtained function does not have a positive second derivative anywhere in the high-rigidity (>1 GV) range since the differential SEP fluence is not expected to increase with R in this range.

This is quantified as the condition that $R_2 > 0, \gamma_2 > 0$ or, for $\gamma_2 \leq 0$, we required that $R_2 (\sqrt{-\gamma_2} - \gamma_2) < 1$. We also required the formal fit to exceed none of the m upper limits. Fits that did not satisfy these conditions were discarded, and the corresponding Monte Carlo simulation was redone without counting it in the statistic. The obtained best-fit set of parameters ($J_{2,l}$, $\gamma_{2,l}$, and $R_{2,l}$) was fixed and used in Step 2.

Step 2: Fitting the low-energy part

The set of N low-energy ($R < 1$ GV) fluences $F^*(R^*)$ was obtained in a similar way to Step 1, assuming a fixed value of the uncertainty being 10% (20% for the pre-GOES/HEPAD era before 1989)⁴ of the tabulated value and applying the uniform distribution. Only points with $R > 168$ MV (corresponding to energy above 15 MeV for protons) were considered, since SEPs with the energy < 15 MeV may have different sources and different spectral parameters (e.g. Reames 1999; Cliver 2016).

Next, each of these $F^*(R^*)$ values was divided by the extrapolated function obtained in Step 1 to form a set of values $X(R^*)$:

$$X(R^*) = \frac{F^*(R^*)}{J_2 (R^*/1\text{GV})^{-\gamma_2} \cdot \exp(-R^*/R_2)}. \quad (5)$$

The obtained set of points $X(R^*)$ was fitted using the same non-linear least-squares method as in Step 1, with the following function:

$$x(R) = \left(\frac{R}{\gamma_0 R_0} \right)^{-\gamma_0} \exp \left(-\frac{R}{R_0} + \gamma_0 \right), \quad (6)$$

which can be obtained by dividing the low-rigidity part of MBF (Equation 1) by its high-rigidity part (Equation 2). We checked that the obtained fit parameters are mathematically reasonable, so the best-fit function does not have a positive derivative anywhere, since the integral fluence cannot increase with R . This condition is quantified as $\gamma_1/R + 1/R_1 > 0$ for the rigidity range from 137 MV (equivalent to 10 MeV energy) to R_b .

Thus, for each l -th iteration, a set of parameters $J_{2,l}$, $\gamma_{2,l}$, $\gamma_{1,l}$, $R_{2,l}$, $R_{1,l}$ was calculated for an analysed event. Then, the formal χ_l^2 value was computed as the merit function between the fitted curve \mathcal{F} and the data points $F(R)$:

$$\chi_l^2 = \sum_{i=1}^{M+N} \left(\frac{\mathcal{F}_i(R_i) - F_i(R_i)}{\sigma_i} \right)^2. \quad (7)$$

This set of parameters and the value of χ_l^2 were recorded for the l -th iteration, and then a new $(l+1)$ -st iteration started.

This procedure was repeated $L = 5000$ times, and the best-fit parameters corresponding to the minimum (among all L iterations) value of χ_{\min}^2 were saved and used in the next step of the procedure. We also checked points for outliers. If any data point contributed more than 100 to the total χ^2 of the best-fit option (i.e. laying beyond 10σ from the best-fit curve), such a data point was discarded and the fit redone for that event. Only one outlier of this kind was found – the point corresponding to the fluence of protons with energy > 360 MeV for GLE #24 from Webber et al. (2007). The set of parameters corresponding to the χ_{\min}^2 was selected as the best-fit set and used in Step 3.

⁴ This is an ad-hoc order-of-magnitude estimate based on the possibility of drawing a smooth curve throughout the experimental points within the error bars, or, on other words, keeping the best-fit merit function χ_{\min}^2 (Figure 2) of the order of unity per degree of freedom.

Step 3: Evaluation of the uncertainties of the parameters

Next, we performed an additional Monte Carlo study of the uncertainties of the obtained best-fit parameters. The value of each parameter was varied randomly (and independently of each other) so that the new value of a parameter P (any of the five parameters of the MBF) was taken as

$$P^* = P_0 \cdot (1 + r), \quad (8)$$

where P_0 is the best-fit value found in Steps 1 and 2, and r is a normally distributed pseudo-random number with a zero mean and the standard deviation of 0.5. All five parameters of the MBF were simultaneously and independently randomised in this way. If these parameters were not rejected by the physical-criteria checks (described in Steps 1 and 2), the formal χ^2 value (Equation 7) was calculated for the corresponding MBF and the data points. If the obtained χ^2 value did not exceed $\chi_{\min}^2 + 5.89$, the corresponding set of parameters was recorded as being within a 68% confidence interval (c.i.) for a five-parameter model (e.g. Chapter 15.6 of Press et al. 2007), otherwise it was discarded and the simulation was redone. If a value of $\chi^2 < \chi_{\min}^2$ was obtained during this step, it was assigned as a new χ_{\min}^2 , and the values of the best-fit parameters P_0 reset, and Step 3 was restarted anew. This procedure was repeated 10000 times for each analysed event, which involved (including the discarded iterations) $3 \cdot 10^8$ iterations for GLE #5, shown in Figure 2.

Figure 2 shows an example of such an analysis. Similar plots were constructed and analysed for all the studied events. The bottom row of panels depicts the relations between the χ^2 value and the value of each of the five parameters. Each panel contains 10000 points satisfying the condition of $\chi^2 \leq \chi_{\min}^2 + 5.89$ (see above). One can see that the relations have the inverted (generally asymmetric) bell-shaped profile, clearly defining the uncertainties for each of the parameter. The corresponding ranges of the MBF fits are shown as grey shaded areas in Figure 1 and Appendix A. However, it would be incorrect to provide 68% c.i. uncertainties for each parameter independently, since some of them are tightly interrelated (e.g. γ_1 and R_1 , and γ_2 , R_2 and J_2), as can be seen in Figure 2. We found that the two parts of the MBF (Equations 1 and 2) can be considered independent (see Figure 2 (b, c, d, e, g, h)), but within each part, the parameters' values are highly correlated (a, f, i, j). As the key parameters, we consider γ_1 and γ_2 , which are not fully independent in the statistical sense (the Pearson's correlation coefficient between them is 0.2), but the power of their common variability is only 4%, and thus their uncertainties can be assumed as roughly independent. Confidence interval (68%) uncertainties for γ_1 and γ_2 are given in the CDS table. Uncertainties of other parameters are related to these two key parameters and cannot be considered independent (Pearson's correlation coefficients are statistically significant, ranging from 0.86 to 0.96). Accordingly, the uncertainties of other parameters can be calculated from those of γ_1 and γ_2 . The overall quality of the spectral fit can be evaluated via the range δF defined as the average ratio:

$$\delta F = 100 \% \times \left\langle \frac{F_{\text{up}}(R) - F_{\text{low}}(R)}{F_{\text{up}}(R) + F_{\text{low}}(R)} \right\rangle_{R_s < R < R_n}, \quad (9)$$

where $F_{\text{up}}(R)$ and $F_{\text{low}}(R)$ are the upper and lower bound values of the MBF for all combinations of the parameters within the 68% c.i. range ($\chi_{\min}^2 + 5.89$ – see Figure 2) for each value of rigidity R ; this is depicted as the upper and lower envelopes of the grey area in Figure 1, and the averaging is performed in the

(logarithmically sampled) rigidity range from the lowest rigidity R_s for the space-borne data point (typically 230 MV), to the highest rigidity R_n of non-zero NM data points. The obtained best-fit MBF parameters (R_2 values exceeding 100 GV are given as $+\infty$), along with the 68% uncertainties of the key parameters γ_1 and γ_2 , as well as the values of δF for the analysed events are summarised in Table 2 and provided in a readable format in CDS. CDS also contains numerical values of SEP fluences calculated using the obtained best-fit parameters. We note that the obtained best-fit spectra are not recommended to be extrapolated to energies below 30 MeV (i.e. beyond the energy range used for the fit) as this can lead to unphysical results in the low-energy range.

4. Conclusions

In this work, event-integrated fluences of solar energetic particles were re-evaluated for most major SEP events (GLEs) using updated low-energy flux estimates, greatly improved high-energy flux data, and the newly developed reconstruction methods. The earlier estimates (Tylka & Dietrich 2009; Raukunen et al. 2018) were essentially revisited here, providing an accurate parametrisation of the rigidity spectra, with the spectral parameters being tabulated in Table 2 and provided in CDS. In particular, it was shown earlier (Usoskin et al. 2020b, Fig. 6) that the Band function spectral shape can lead to a significant overestimate of the high-energy tail of the spectrum, and a strong roll-off (assumed to be exponential here) is required. Accordingly, for the parametrisation of the spectral fluence shape, we propose a modified Band function (Equations 1–2), which is a combination of the standard Band and a modified Ellison-Ramaty functions. The spectral fluences evaluated with the revisited datasets and a new method form a solid basis for more precise studies of the physics of solar eruptive events and the transport of energetic particles in the interstellar medium.

The new spectral fluences will be also useful in various applications of SEP influence on terrestrial effects such as cosmic-ray-induced ionisation (e.g., Jackman et al. 2008; Usoskin et al. 2011; Duderstadt et al. 2016), radiation hazards (e.g., Feynman et al. 1993; Jiggins et al. 2014; Mishev et al. 2015; Raukunen et al. 2018), or cosmogenic isotope production (Webber et al. 2007; Kovaltsov et al. 2014; Mekhaldi et al. 2015). The latter is of particular importance for studies of the reference SEP events (Cliver et al. 2014; Usoskin et al. 2020a), and, accordingly, to a more precise assessment of historical extreme solar particle storms (Miyake et al. 2019).

Acknowledgements. Detrended data of GLE recorded by NMs were obtained from the International GLE database <https://gle.oulu.fi>. PIs and teams of all the ground-based neutron monitors and space-borne experiments whose data were used here are gratefully acknowledged. This work was partially supported by the Academy of Finland (project No. 321882 ESPERA). Collection of the data from cosmic-ray/ionospheric experiments before 1989 and the creation of full dataset used in this work was supported by the Russian Science Foundation project no. 20-72-10170. Development of the fluence fitting procedure was supported by the Russian Science Foundation project no. 20-67-46016. The work in the University of Turku was performed in the framework of the Finnish Centre of Excellence in Research of Sustainable Space funded by the Academy of Finland (grant no. 312357). The authors benefited from discussions within the ISSI International Team work (HEROIC team) and ISWAT-COSPAR S1-02 team.

References

- Adriani, O., Barbarino, G. C., Bazilevskaya, G. A., et al. 2014, Phys. Rep., 544, 323

Table 2. List of the analysed GLE events and best-fit parameters of the modified Band function (Equations 1 and 2), as well as the 68 % uncertainty of the fit δF . $+\infty$ implies the value greater than 100 GV. Parameter J_1 can be calculated using Equation 3.

GLE #	Date	γ_1	R_1 , GV	J_2 , cm ⁻²	γ_2	R_2 , GV	R_b , GV	Δ , %
5	23-Feb-1956	1.59	0.770	$1.63 \cdot 10^8$	4.84	8.614	2.748	21.0
8	04-May-1960	2.85	-1.276	$9.43 \cdot 10^5$	-1.36	0.507	1.528	33.8
10	12-Nov-1960	3.82	6.244	$2.71 \cdot 10^7$	0.01	0.483	1.995	17.0
11	15-Nov-1960	2.52	0.603	$4.20 \cdot 10^7$	7.26	34.807	2.909	17.5
12	20-Nov-1960	1.71	0.312	$3.73 \cdot 10^5$	5.77	$+\infty$	1.267	29.0
13	18-Jul-1961	1.81	0.231	$2.60 \cdot 10^6$	4.28	0.977	0.747	29.8
16	28-Jan-1967	1.98	0.522	$2.12 \cdot 10^6$	4.90	4.630	1.718	17.5
18	29-Sep-1968	-2.68	0.050	$2.39 \cdot 10^4$	4.68	$+\infty$	0.368	32.4
19	18-Nov-1968	3.97	0.433	$1.42 \cdot 10^5$	5.73	10.705	0.794	32.8
20	25-Feb-1969	-0.03	0.124	$1.57 \cdot 10^5$	4.47	5.555	0.571	27.0
21	30-Mar-1969	1.57	0.540	$9.76 \cdot 10^5$	3.00	1.653	1.147	19.4
22	24-Jan-1971	6.07	-0.408	$6.72 \cdot 10^5$	3.84	1.352	0.699	24.5
23	01-Sep-1971	2.89	1.172	$1.19 \cdot 10^7$	2.09	0.427	0.537	24.1
24	04-Aug-1972	2.02	0.152	$4.35 \cdot 10^6$	11.96	$+\infty$	1.511	26.7
25	07-Aug-1972	1.53	0.039	$2.60 \cdot 10^5$	5.07	$+\infty$	0.138	21.5
26	29-Apr-1973	-0.18	0.098	$4.32 \cdot 10^4$	3.96	53.011	0.406	39.3
27	30-Apr-1976	3.06	0.566	$1.02 \cdot 10^5$	5.89	$+\infty$	1.602	43.6
28	19-Sep-1977	5.49	-0.288	$2.71 \cdot 10^7$	0.03	0.185	0.615	35.8
29	24-Sep-1977	2.34	0.558	$2.40 \cdot 10^5$	4.78	$+\infty$	1.362	26.5
30	22-Nov-1977	4.72	-0.346	$7.03 \cdot 10^5$	2.93	1.349	0.493	18.9
31	07-May-1978	4.27	-1.585	$3.14 \cdot 10^4$	0.02	1.175	2.868	23.3
32	23-Sep-1978	6.42	-0.171	$3.50 \cdot 10^5$	4.14	3.222	0.370	24.3
33	21-Aug-1979	5.94	-1.006	$2.11 \cdot 10^5$	0.11	0.383	1.617	30.5
35	10-May-1981	4.65	-13.452	$6.45 \cdot 10^{11}$	-15.17	0.059	1.164	49.1
36	12-Oct-1981	7.40	-0.158	$5.59 \cdot 10^5$	3.35	2.857	0.606	28.3
37	26-Nov-1982	4.90	-0.976	$6.99 \cdot 10^4$	1.67	1.287	1.793	26.8
38	07-Dec-1982	5.96	-0.250	$8.58 \cdot 10^5$	2.05	0.922	0.769	27.3
39	16-Feb-1984	3.76	-29.660	$1.30 \cdot 10^5$	0.21	0.715	2.479	31.6
40	25-Jul-1989	-0.24	0.154	$7.33 \cdot 10^4$	6.18	$+\infty$	0.989	26.0
41	15-Aug-1989	2.10	0.315	$1.65 \cdot 10^6$	4.25	1.375	0.879	15.0
42	29-Sep-1989	-1.95	0.069	$9.89 \cdot 10^6$	3.39	5.935	0.373	9.6
43	19-Oct-1989	-1.21	0.109	$6.59 \cdot 10^6$	4.44	2.960	0.639	13.5
44	22-Oct-1989	0.35	0.122	$1.84 \cdot 10^6$	6.07	5.807	0.713	15.6
45	24-Oct-1989	-1.77	0.077	$1.19 \cdot 10^7$	2.95	1.131	0.390	13.0
46	15-Nov-1989	-1.16	0.117	$5.58 \cdot 10^4$	4.97	$+\infty$	0.717	20.4
47	21-May-1990	-1.55	0.088	$2.85 \cdot 10^5$	4.06	$+\infty$	0.494	12.4
48	24-May-1990	-0.95	0.137	$6.14 \cdot 10^5$	4.08	7.501	0.702	15.9
49	26-May-1990	-1.03	0.131	$2.80 \cdot 10^5$	4.51	$+\infty$	0.726	14.8
50	28-May-1990	-0.80	0.142	$1.67 \cdot 10^5$	5.51	$+\infty$	0.900	21.1
51	11-Jun-1991	-2.31	0.059	$1.55 \cdot 10^5$	4.87	$+\infty$	0.424	14.2
52	15-Jun-1991	1.13	0.200	$8.92 \cdot 10^5$	5.02	2.883	0.836	15.4
53	25-Jun-1992	2.12	0.297	$8.89 \cdot 10^4$	5.28	$+\infty$	0.939	22.8
55	06-Nov-1997	0.75	0.165	$9.66 \cdot 10^5$	4.23	3.077	0.607	15.6
56	02-May-1998	1.57	0.221	$6.26 \cdot 10^4$	5.01	$+\infty$	0.760	25.9
58	24-Aug-1998	4.60	-0.277	$1.55 \cdot 10^6$	1.65	0.300	0.425	27.5
59	14-Jul-2000	2.80	0.276	$3.46 \cdot 10^6$	5.85	2.191	0.963	17.7
60	15-Apr-2001	1.02	0.290	$2.90 \cdot 10^6$	4.57	3.321	1.128	15.7
61	18-Apr-2001	2.37	0.547	$3.68 \cdot 10^5$	4.01	5.172	1.003	20.5
62	04-Nov-2001	3.70	0.311	$3.08 \cdot 10^5$	6.63	$+\infty$	0.911	18.6
63	26-Dec-2001	2.45	0.245	$5.79 \cdot 10^5$	4.11	0.673	0.640	20.7
64	24-Aug-2002	2.09	0.281	$1.69 \cdot 10^5$	7.00	$+\infty$	1.380	33.9
65	28-Oct-2003	6.49	-0.525	$5.31 \cdot 10^6$	0.01	0.447	1.565	22.0
66	29-Oct-2003	1.56	0.188	$5.19 \cdot 10^5$	6.85	$+\infty$	0.995	23.9
67	02-Nov-2003	3.62	0.541	$1.81 \cdot 10^5$	5.40	$+\infty$	0.963	20.6
69	20-Jan-2005	1.16	0.295	$8.03 \cdot 10^6$	4.73	2.392	1.201	16.3
70	13-Dec-2006	0.18	0.114	$1.46 \cdot 10^6$	3.77	1.449	0.444	14.5
71	16-May-2012	2.23	0.372	$2.60 \cdot 10^5$	7.03	24.488	1.813	10.5
72	10-Sep-2017	1.46	0.164	$4.59 \cdot 10^5$	6.31	$+\infty$	0.795	20.9

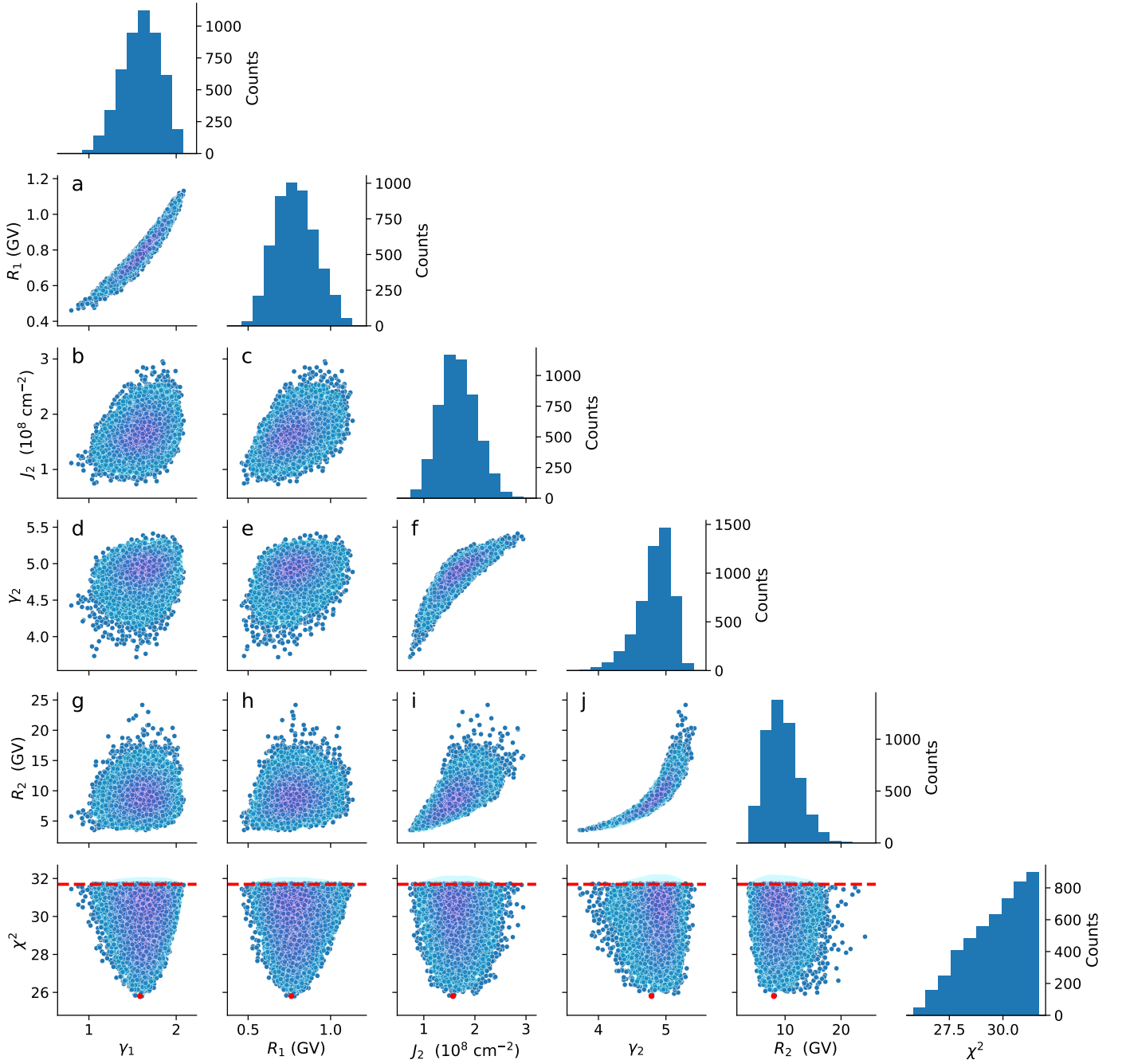


Fig. 2. Distribution of the parameters and their pair-wise correlations for the MBF fitting of the GLE #5 obtained for 10000 iterations (see Step 3 in Section 3). The red dots in the bottom panels correspond to the minimum χ^2_{\min} , while the horizontal red dashed line $\chi^2 = \chi^2_{\min} + 5.89$ denotes the 68% confidence interval for the best-fit parameter values. Colour intensity corresponds to the point density. The diagonal panels depict histograms of the parameter values' distribution.

Aguilar, M., Ali Cavazonza, L., Alpat, B., et al. 2018, *Phys. Rev. Lett.*, 121, 051101
 Anastasiadis, A., Lario, D., Papaioannou, A., Kouloumvakos, A., & Vourlidas, A. 2019, *Philos. T. R. Soc. A*, 377, 20180100
 Asvestari, E., Gil, A., Kovaltsov, G. A., & Usoskin, I. G. 2017, *J. Geophys. Res. (Space Phys.)*, 122, 9790
 Band, D., Matteson, J., Ford, L., et al. 1993, *Astrophys. J.*, 413, 281
 Bazilevskaya, G. A., Cliver, E. W., Kovaltsov, G. A., et al. 2014, *Space Sci. Rev.*, 186, 409
 Bindi, V. 2017, *Adv. Space Res.*, 60, 753
 Bruno, A., Bazilevskaya, G. A., Boezio, M., et al. 2018, *Astrophys. J.*, 862, 97
 Clem, J. & Dorman, L. 2000, *Space Sci. Rev.*, 93, 335
 Cliver, E. W. 2016, *Astrophys. J.*, 832, 128
 Cliver, E. W., Hayakawa, H., Love, J. J., & Neidig, D. F. 2020, *Astrophys. J.*, 903, 41

Cliver, E. W., Tylka, A. J., Dietrich, W. F., & Ling, A. G. 2014, *Astrophys. J.*, 781, 32
 Desai, M. & Giacalone, J. 2016, *Liv. Rev. Solar Phys.*, 13, 3
 Duderstadt, K. A., Dobb, J. E., Schwadron, N. A., et al. 2016, *J. Geophys. Res. (Atmos.)*, 121, 2994
 Ellison, D. C. & Ramaty, R. 1985, *Astrophys. J.*, 298, 400
 Feynman, J. & Gabriel, S. 1990, *Solar Phys.*, 127, 393
 Feynman, J., Spitale, G., Wang, J., & Gabriel, S. 1993, *J. Geophys. Res.*, 98, 13
 Forbush, S. E. 1946, *Phys. Rev.*, 70, 771
 Goswami, J., McGuire, R., Reedy, R., Lal, D., & Jha, R. 1988, *J. Geophys. Res.*, 93, 7195
 Herbst, K., Grenfell, J. L., Sinnhuber, M., et al. 2019, *Astron. Astrophys.*, 631, A101
 Jackman, C. H., Marsh, D. R., Vitt, F. M., et al. 2008, *Atmos. Chem. Phys.*, 8, 765

- Jiggins, P., Chavy-Macdonald, M.-A., Santin, G., et al. 2014, *J. Space Weather Space Clim.*, 4, A20
- Jun, I., Swimm, R. T., Ruzmaikin, A., et al. 2007, *Adv. Space Res.*, 40, 304
- King, J. 1974, *J. Spacecraft Rockets*, 11, 401
- Klein, K.-L. & Dalla, S. 2017, *Space Sci. Rev.*, 212, 1107
- Kocharov, L., Pohjolainen, S., Mishev, A., et al. 2017, *Astrophys. J.*, 839, 79
- Koldobskiy, S. A., Kovaltsov, G. A., Mishev, A. L., & Usoskin, I. G. 2019, *Solar Phys.*, 294, 94
- Koldobskiy, S. A., Kovaltsov, G. A., & Usoskin, I. G. 2018, *Solar Phys.*, 293, 110
- Kong, X., Guo, F., Giacalone, J., Li, H., & Chen, Y. 2017, *Astrophys. J.*, 851, 38
- Kouloumvakos, A., Nindos, A., Valtonen, E., et al. 2015, *Astron. Astrophys.*, 580, A80
- Kovaltsov, G. A., Usoskin, I. G., Cliver, E. W., Dietrich, W. F., & Tylka, A. J. 2014, *Solar Phys.*, 289, 4691
- Mekhaldi, F., Muscheler, R., Adolphi, F., et al. 2015, *Nature Comm.*, 6, 8611
- Mishev, A., Adibpour, F., Usoskin, I., & Felsberger, E. 2015, *Adv. Space Res.*, 55, 354
- Mishev, A., Koldobskiy, S., Kovaltsov, G., Gil, A., & Usoskin, I. 2020, *J. Geophys. Res. (Space Phys.)*, 125, e2019JA027433
- Mishev, A., Usoskin, I., & Kovaltsov, G. 2013, *J. Geophys. Res. (Space Phys.)*, 118, 2783
- Mishev, A., Usoskin, I., Raukunen, O., et al. 2018, *Solar Phys.*, 293, 136
- Miyake, F., Usoskin, I., & Poluianov, S., eds. 2019, *Extreme Solar Particle Storms: The Hostile Sun* (Bristol, UK: IOP Publishing)
- Onsager, T., Grubb, R., Kunches, J., et al. 1996, in *GOES-8 and Beyond*, ed. E. R. Washwell, Vol. 2812 (SPIE), 281–290
- Plainaki, C., Mavromichalaki, H., Laurenza, M., et al. 2014, *Astrophys. J.*, 785, 160
- Press, W., Teukolsky, S., Vetterling, W., & Flannery, B. 2007, *Numerical Recipes 3rd Edition: The Art of Scientific Computing*, 3rd edn. (USA: Cambridge University Press)
- Raukunen, O., Paassilta, M., Vainio, R., et al. 2020, *J. Space Weather Space Clim.*, 10, 24
- Raukunen, O., Vainio, R., Tylka, A. J., et al. 2018, *J. Space Weather Space Clim.*, 8, A04
- Reames, D. V. 1999, *Space Sci. Rev.*, 90, 413
- Reedy, R. 1977, in *Lunar and Planetary Science VIII*, ed. R. Merrill (Houston, U.S.A.: Lunar and Planetary Institute), 825–839
- Reeves, G., Cayton, T., Gary, S., & Belian, R. 1992, *J. Geophys. Res.*, 97, 6219
- Sellers, F. B. & Hanser, F. A. 1996, in *GOES-8 and Beyond*, ed. E. R. Washwell, Vol. 2812 (SPIE), 353–364
- Shea, M. A. & Smart, D. F. 2012, *Space Sci. Rev.*, 171, 161
- Tylka, A. & Dietrich, W. 2009, in *31th International Cosmic Ray Conference* (Lódź, Poland: Universal Academy Press), icrc0273
- Tylka, A., Dietrich, W., & Boberg, P. 1997, *IEEE Trans. Nucl. Sci.*, 44, 2140
- Usoskin, I., Koldobskiy, S., Kovaltsov, G., et al. 2020a, *J. Geophys. Res. (Space Phys.)*, 125, e27921
- Usoskin, I., Koldobskiy, S., Kovaltsov, G. A., et al. 2020b, *Astron. Astrophys.*, 640, A17
- Usoskin, I. G., Kovaltsov, G. A., Mironova, I. A., Tylka, A. J., & Dietrich, W. F. 2011, *Atmos. Chem. Phys.*, 11, 1979
- Vainio, R. & Afanasiev, A. 2018, *Astrophys. Space Sci. Lib.*, Vol. 444, *Particle Acceleration Mechanisms*, ed. O. Malandraki & N. Crosby, 45–61
- Vainio, R., Desorgher, L., Heynderickx, D., et al. 2009, *Space Sci. Rev.*, 147, 187
- Van Allen, J. A., Baker, D. N., Randall, B. A., & Sentman, D. D. 1974, *J. Geophys. Res.*, 79, 3559
- Webber, W., Higbie, P., & McCracken, K. 2007, *J. Geophys. Res.*, 112, A10106

Appendix A: Reconstructed integral spectra

Event-integrated fluences for the analysed GLE events are presented in the plots below. Each plot is similar to Figure 1 of the main text in both style and notations. The GLE number and date are shown on the top of the plots. Symbols represent data from different sources, as specified in the legend: blue crosses and vertical lines correspond to data from neutron monitors and upper estimates, respectively, along with their 68% confidence intervals (Usoskin et al. 2020b); coloured dots correspond to space-borne/ionospheric data with the source indicated in the legend ('this work' refers to Table 1); and the dark curve depicts the best-fit modified Band function (Equations 1 and 2; exact values of the parameters are available in Table 2), while the light grey shading represents the 68% confidence interval for the fits (see Step 3 of Section 3).

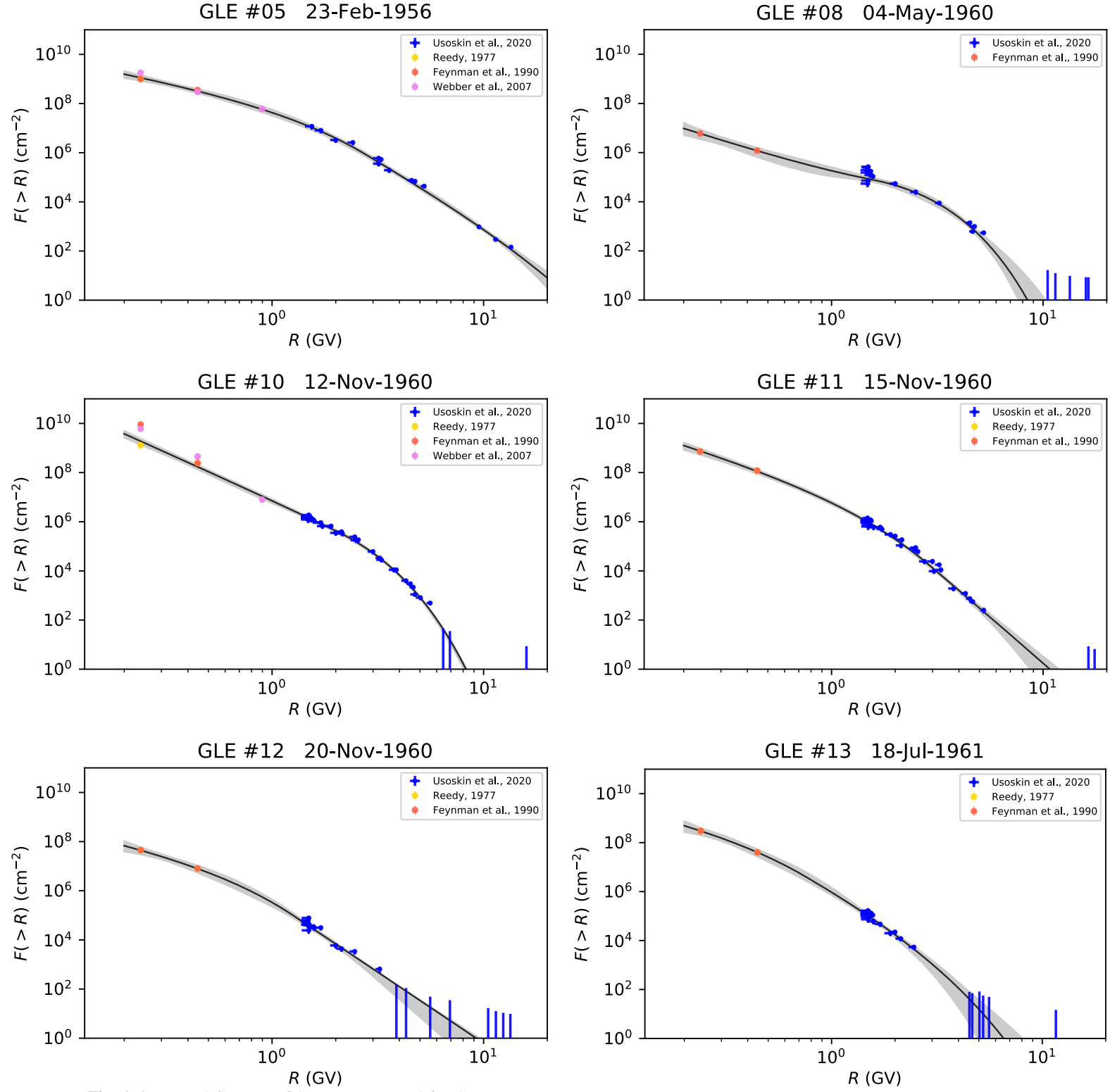


Fig. A.1. Integral fluences of SEP reconstructed for GLEs considered in this work (the GLE number and date are given in the header of each panel). Notations are similar to Fig. 1 of the main text.

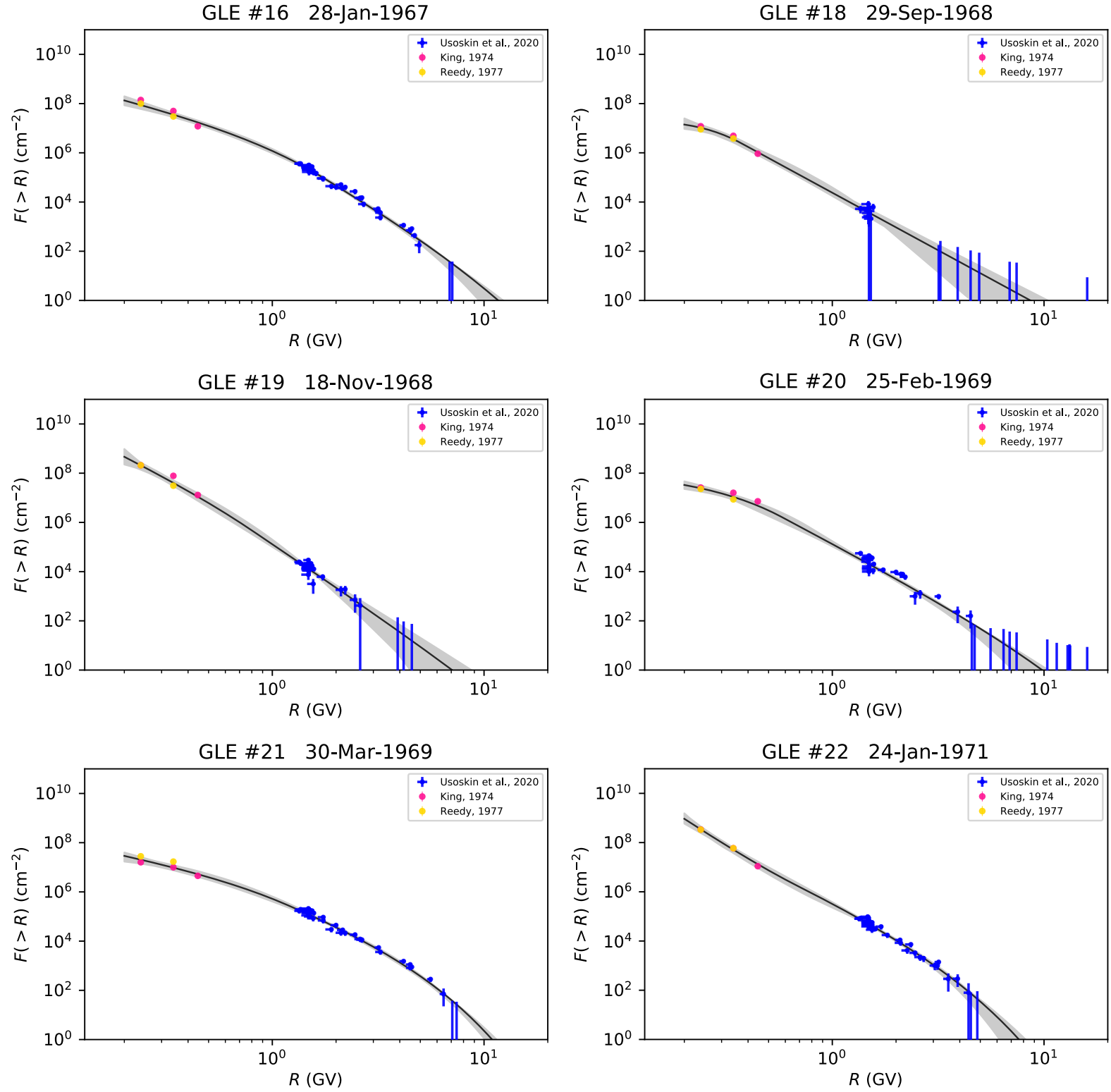


Fig. A.1. Continued

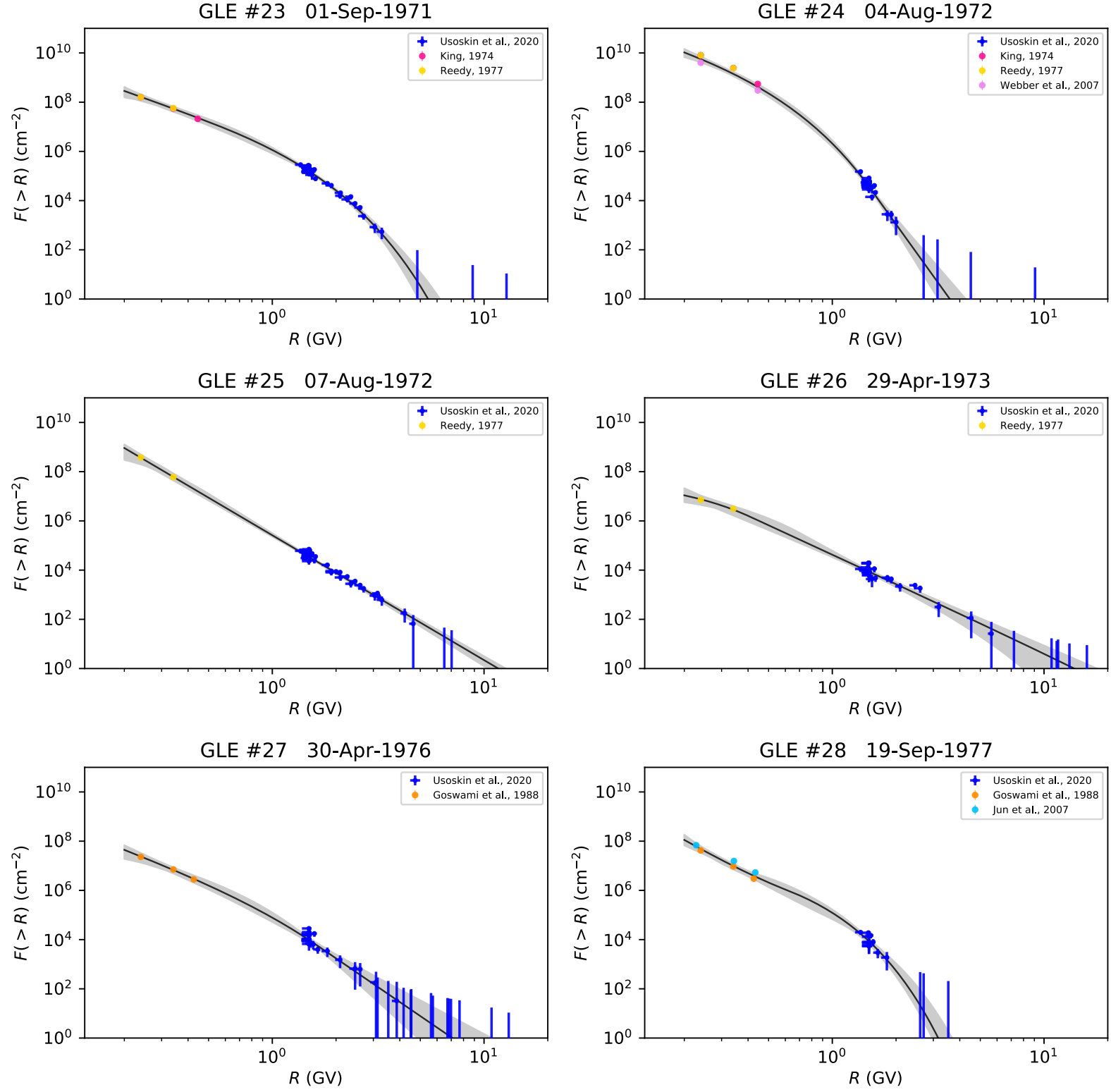


Fig. A.1. Continued

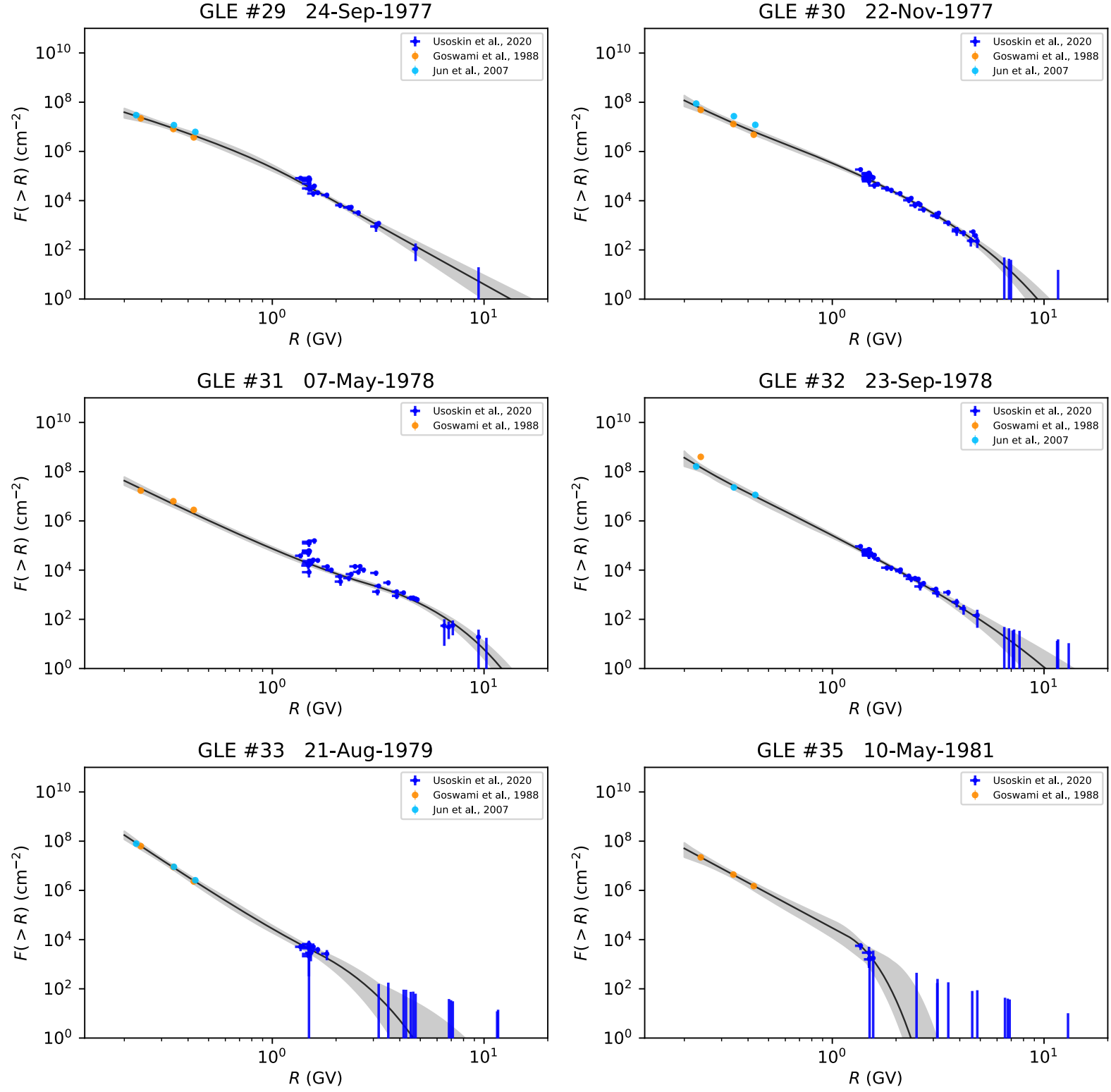


Fig. A.1. Continued

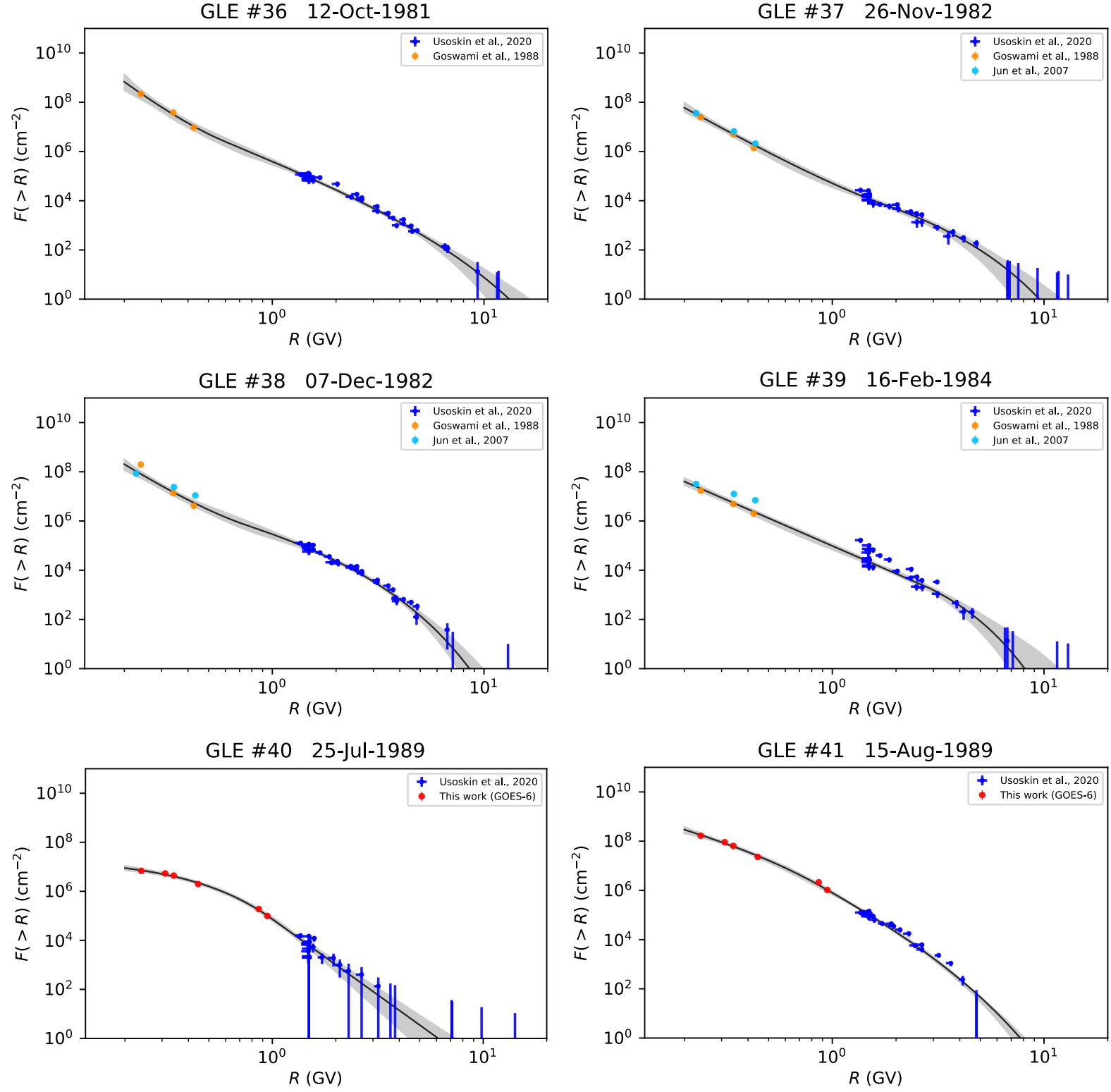


Fig. A.1. Continued

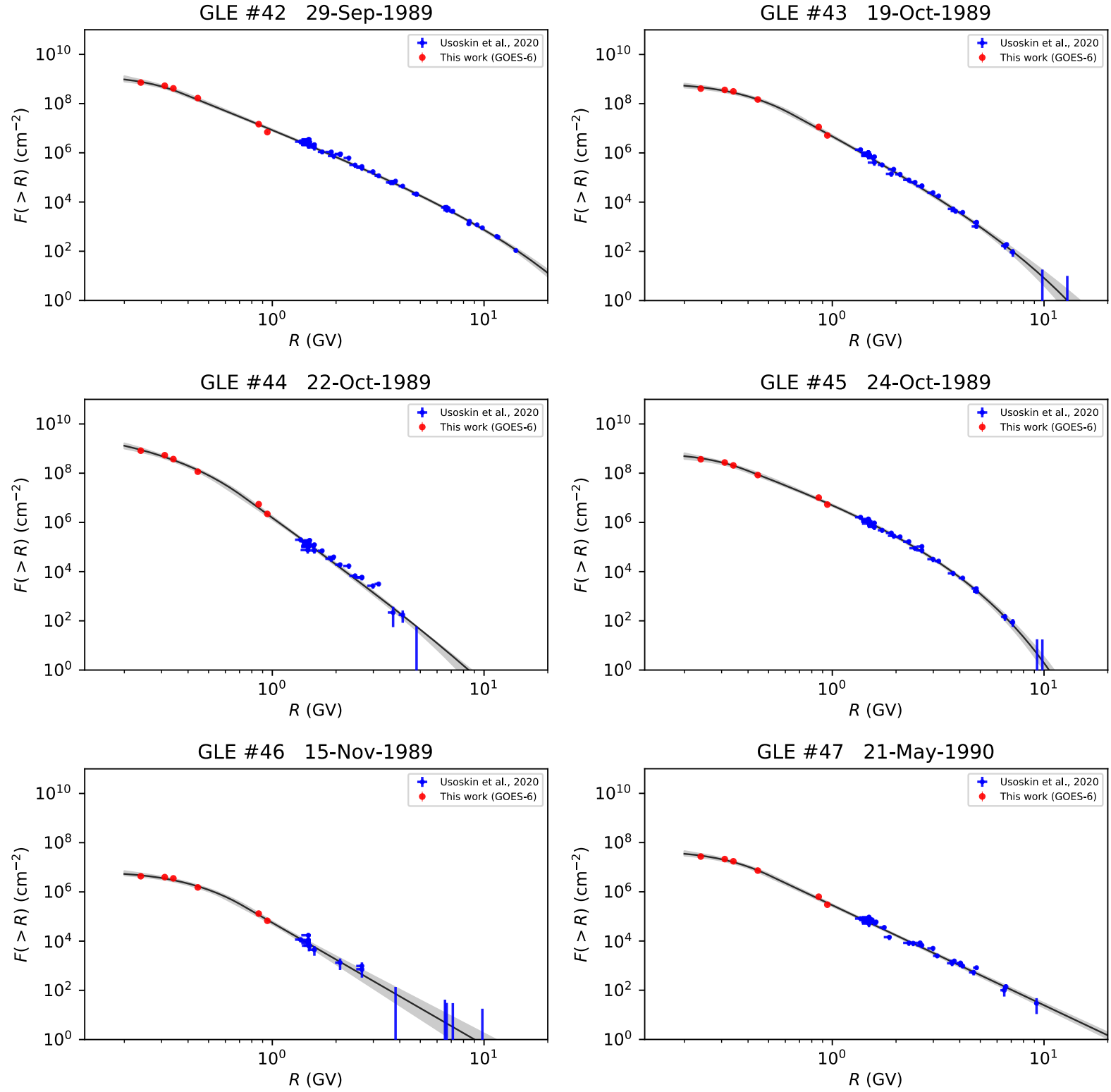


Fig. A.1. Continued

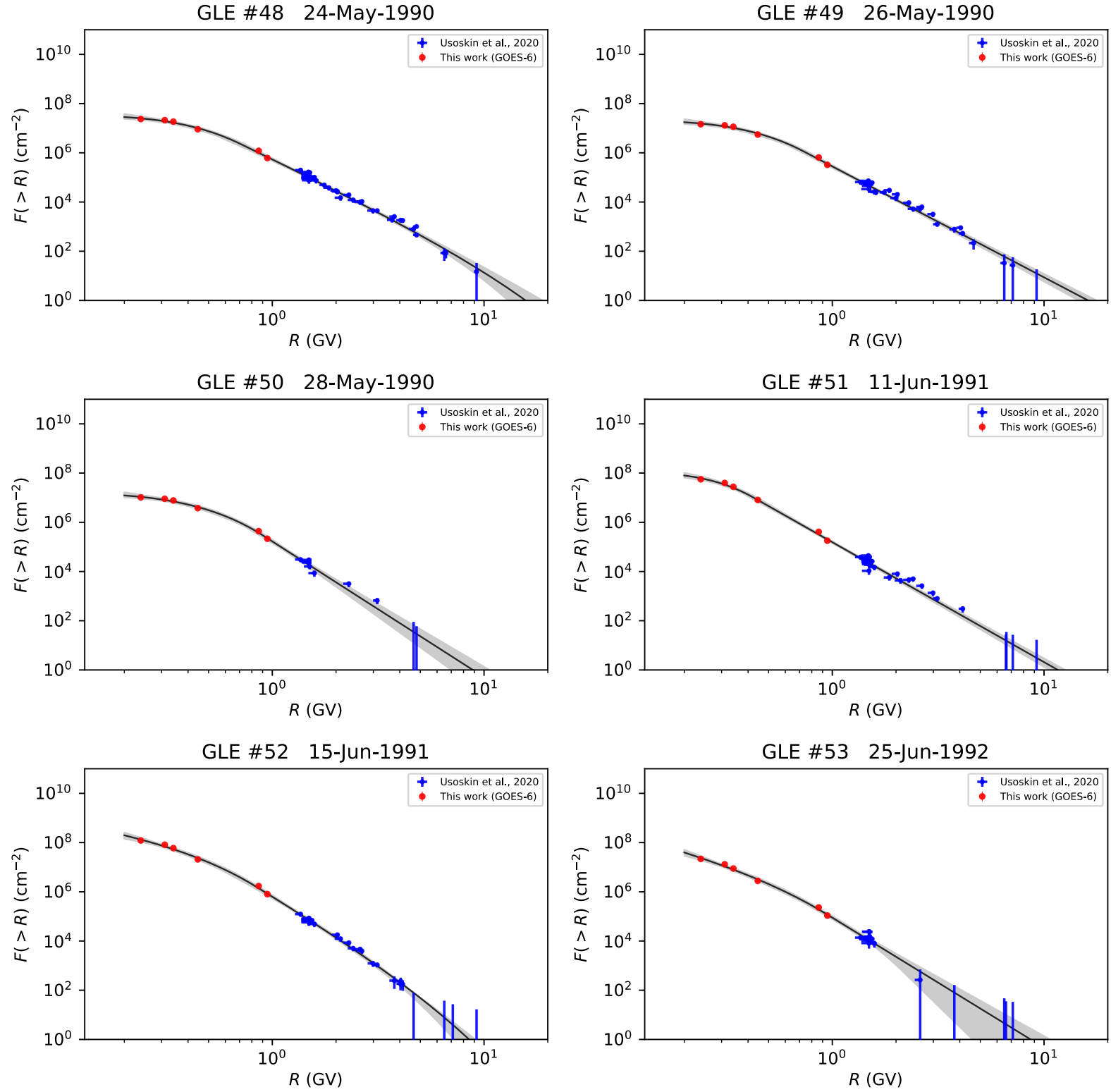


Fig. A.1. Continued

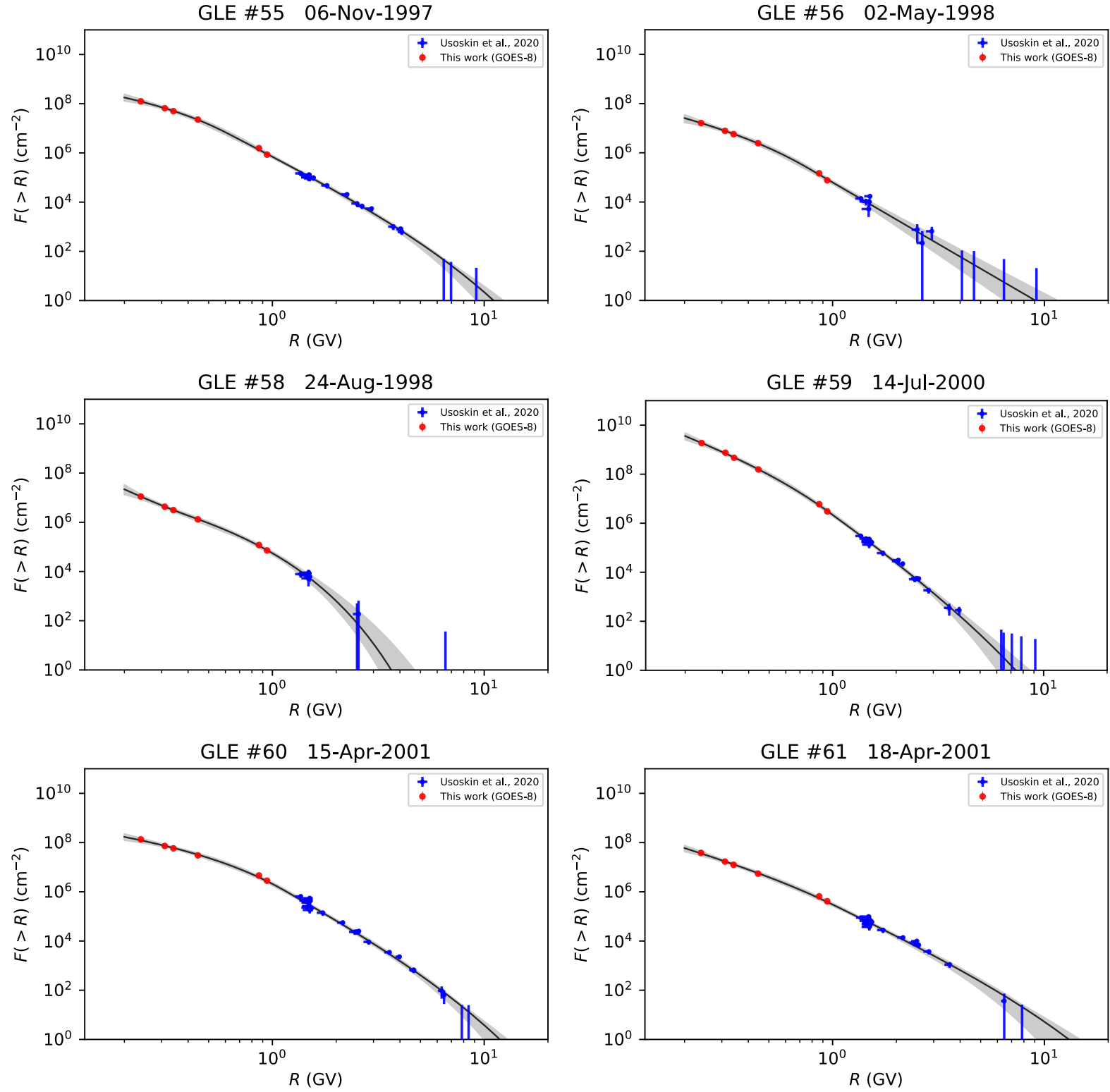


Fig. A.1. Continued

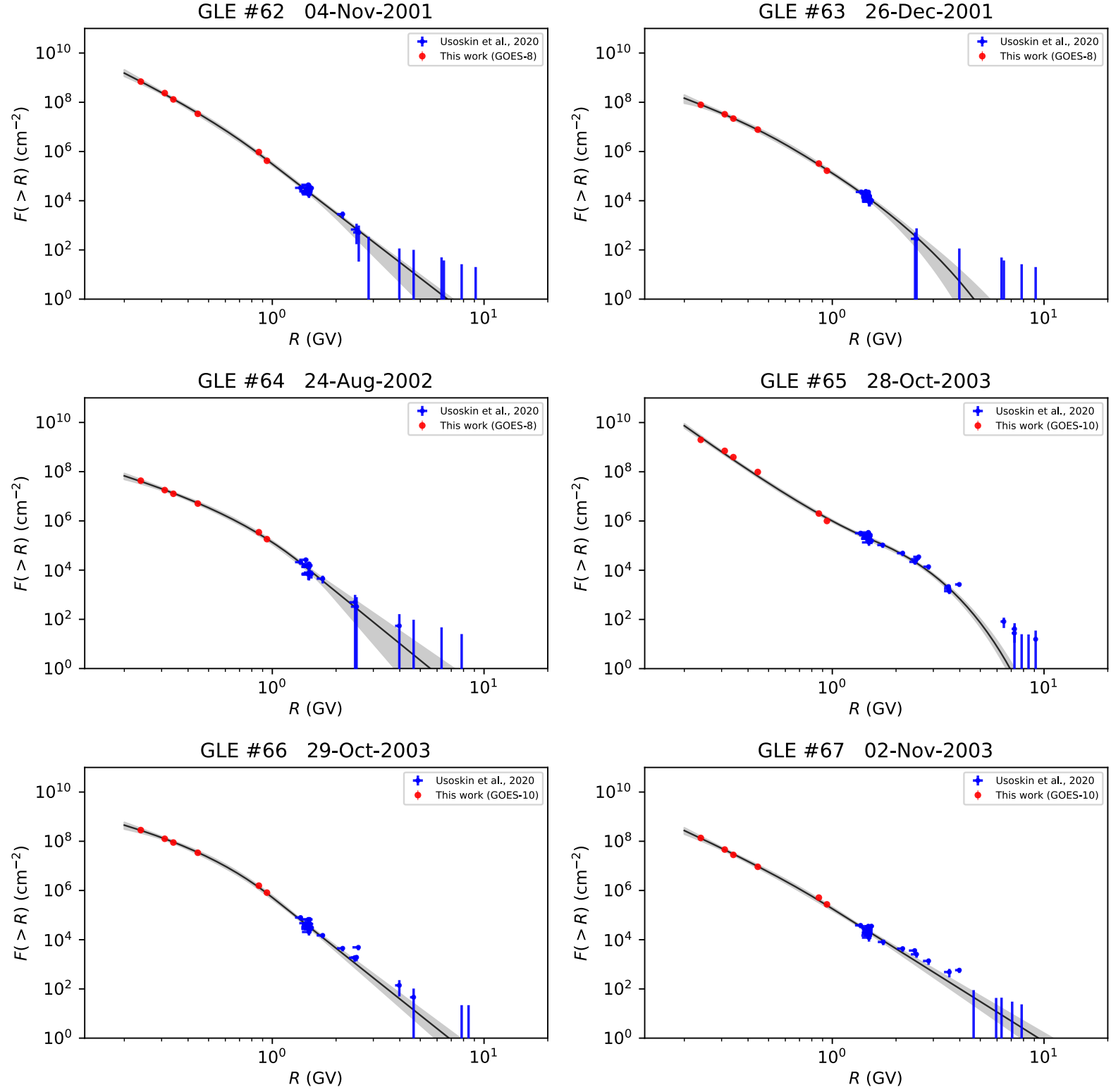


Fig. A.1. Continued

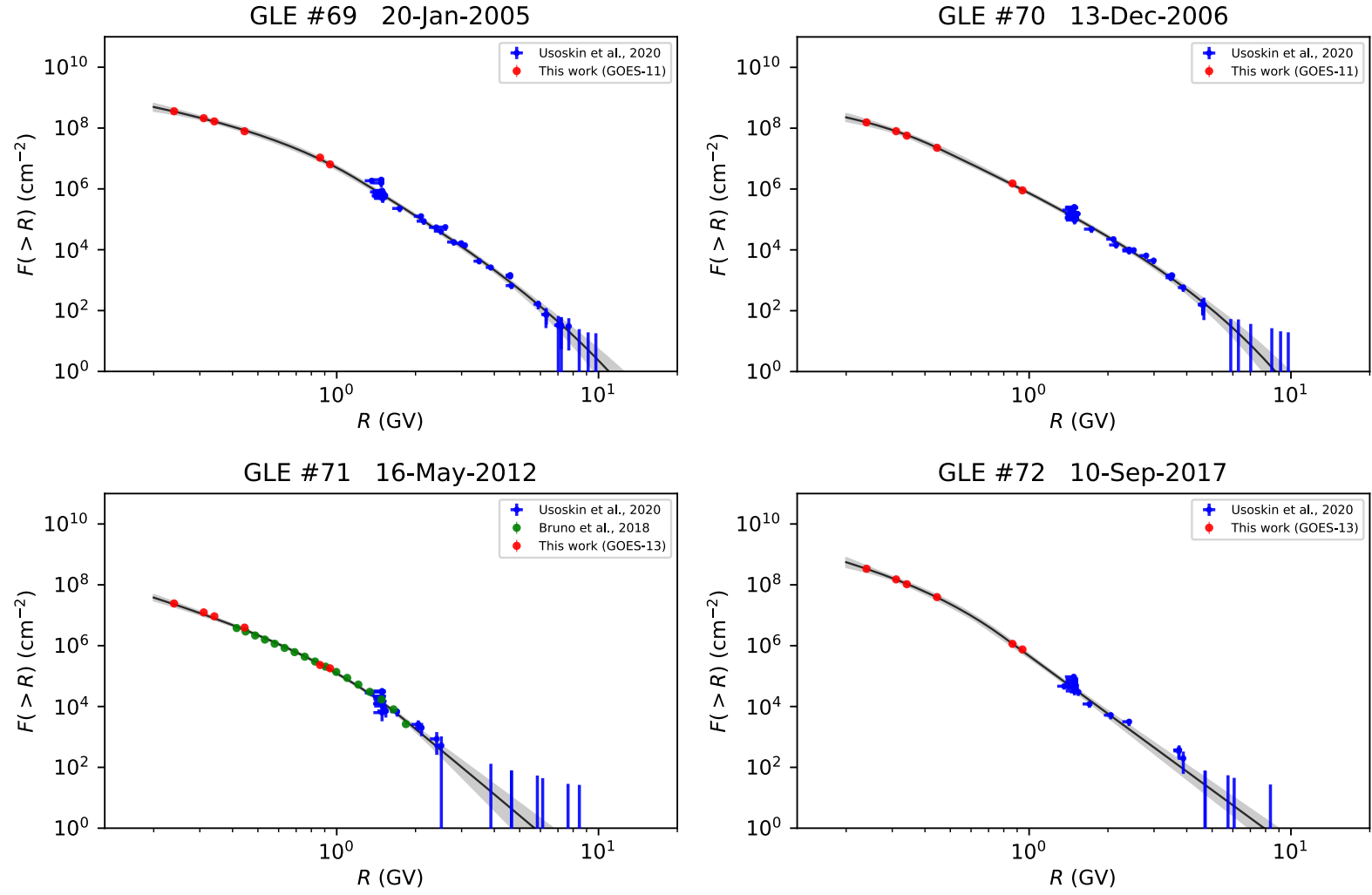


Fig. A.1. Continued